Electric-field-controlled magnetization switching in multiferroic heterostructures containing interactive magnetic nanoislands

IOP Publishing Journal of Physics D: Applied Physics
J. Phys. D: Appl. Phys. **53** (2020) 024002 (9pp) https://doi.org/10.1088/1361-6463/ab4d21

Electric-field-controlled magnetization switching in multiferroic heterostructures containing interactive magnetic nanoislands

Meng-Jun Zhou[1,2], Tiannan Yang[2], Jian-Jun Wang[2,3], Long-Qing Chen[2,3] and Ce-Wen Nan[1,3]

[1] School of Materials Science and Engineering, State Key Lab of New Ceramics and Fine Processing, Tsinghua University, Beijing 100084, People's Republic of China
[2] Department of Materials Science and Engineering, The Pennsylvania State University, University Park, PA 16802, United States of America

E-mail: wjj8384@gmail.com (J-J Wang), lqc3@psu.edu (L-Q Chen) and cwnan@mail.tsinghua.edu.cn (C-W Nan)

Received 14 August 2019, revised 23 September 2019
Accepted for publication 11 October 2019
Published 31 October 2019

Abstract

Switching the magnetization with an electric field in multiferroic heterostructures is desirable since it provides a possibility to achieve information storage with lower power consumption than traditional spintronic devices by using an electric current to drive magnetization rotation. Most of the existing studies, however, have been on multiferroic heterostructures containing either a single magnetic island or spatially well-separated multiple magnetic islands, where the effect of long-range magnetostatic interactions among magnetic islands (i.e. so-called cross-talking) can be ignored. Here we employ phase-field simulations to study the effect of magnetic interactions among islands on the electric-field-controlled magnetization switching in multiferroic heterostructures. As an example, we consider two interactive $Co_{40}Fe_{40}B_{20}$(CoFeB) magnetic nanoislands grown on a PMN-PT ((0 0 1)-oriented $Pb(Mg_{1/3}Nb_{2/3})_{0.7}Ti_{0.3}O_3$) ferroelectric layer. We find that the distance between two neighboring nanoislands has to exceed a critical value to achieve an independent 180° magnetization switching in each nanoisland. The present work provides guidance for further experimental studies on the electric field control of magnetization and design of novel multiferroic devices.

Keywords: multiferroic heterostructures, magnetic domain switching, critical neighboring distance, phase-field modeling

(Some figures may appear in colour only in the online journal)

1. Introduction

Magnetic/ferroelectric multiferroic heterostructures provide a material platform where the electric polarization and magnetization can coexist and couple to each other, thus they are promising candidates for magnetoelectronic devices [1–6]. The coupling between the polarization and magnetization in a multiferroic heterostructure is achieved via the heterointerface between the magnetic and ferroelectric phases. To date, several interfacial coupling mechanisms have been identified, including the charge/orbital modulation [7–9] exchange coupling [10–12] strain-mediated elastic coupling [13–20], charge carrier modulation by the field effect [21, 22], and a recently discovered mechanism by electrically controlled morphology to tune the magnetic properties [23]. Exploiting these coupling mechanisms to achieve electric-field-controlled magnetization switching is desirable, since it may mitigate the energy consumption from Joule heating caused by electric current in most of the existing spintronic devices [24–29].

There have been many experimental and theoretical attempts to achieve electric-field-controlled magnetization switching in multiferroic heterostructures [11, 12, 30–37].

[3] Author to whom any correspondence should be addressed.

Most of them were focused on electric-field-driven 90° magnetization rotation. For example, Hu *et al* studied the 90° magnetization switching induced by an applied voltage in Ni/PMN-PT heterostructures, which was further used to design a magnetoresistive random access memory (MRAM) [33]. The storage capacity of the MRAM proposed by Hu *et al* can be as high as 88 GB per square inches, which was estimated by assuming a lateral size of 64 nm for the magnetic layer. However, in their studies of electric-field-driven magnetization switching and estimation of storage capacity, the interactions among storage units were neglected, which might cause an overestimation of the storage capacity.

In comparison to 90° switching, the electric-field-controlled 180° magnetization switching is more desirable since it can induce larger resistance changes when used in MRAM. By utilizing the synergetic effect from the shape anisotropy and magnetoelastic anisotropy, the electric-field-induced 180° magnetization has been proved to be feasible via both simulations and experiments [26, 27, 38–40]. In particular, by etching a magnetic layer into a nanoisland with a 4-fold symmetry, the magnetization can be switched unidirectionally to complete a 180° full reversal under a pair of tensile and compressive strains transferred from an underneath piezoelectric layer [27]. These earlier studies were also focused on the switching in a single magnetic nanoisland or isolated nanoisland arrays [27, 40–43] grown on a piezoelectric substrate, whereas the cross-talking among magnetic nanoislands was ignored. Therefore, it is still unclear how the interactions among the magnetic nanoislands will affect the magnetization switching in each individual nanoisland. Understanding this interaction is important for the design of multiferroic devices containing densely packed magnetic nanoisland arrays with a small distance between neighboring nanoislands as required for a high memory storage density.

In this work, we employ phase-field simulations to study the electric-field-controlled magnetization switching in multiferroic heterostructures containing two magnetic nanoislands, wherein the magnetostatic interaction between them is incorporated as one of the driving forces to determine the magnetization switching. The phase-field method has been demonstrated as a powerful tool to study the microstructure evolution and properties of materials [44–48] by solving the time-dependent evolution and equilibrium equations, such as the investigation of magnetic or ferroelectric domain structures and domain switching [49, 50], particularly in magnetic/ferroelectric multiferroic heterostructures [51–53]. It has also been extensively employed to calculate the temperature-strain [54–57], strain–strain [56–58] and strain-composition [55] phase-diagrams for ferroelectric materials and magnetic materials.

Here, we use a CoFeB/PMN-PT multiferroic heterostructure as an example (see figure 1(a)) to show the effect of interaction between the two neighboring nanoislands on the magnetization switching in each individual nanoisland. The CoFeB/PMN-PT multiferroic heterostructure has been extensively employed to study the electric-field-controlled magnetization switching [16, 59–64]. As shown in figure 1(a), the two CoFeB magnetic nanoislands, named as magnet *A* and magnet *B*, respectively, are located with a neighboring distances *R* (the distance between the centers of the two magnets). The average magnetization directions in these two magnets are indicated by directional angles ϕ_A and ϕ_B, respectively, as shown in Figure 1(b).

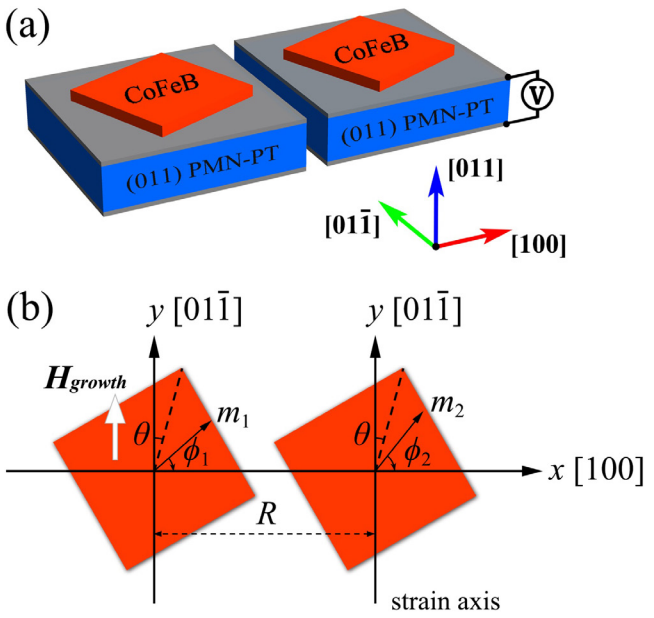

Figure 1. (a) Schematic of the CoFeB/PMN-PT multiferroic heterostructure consisting of two interactive CoFeB magnetic nanoislands on individual (0 1 1) PMN-PT substrates; (b) top view of the multiferroic heterostructure with R representing the distance between the centers of the two neighboring CoFeB magnets, $\mathbf{H}_{\text{growth}}$ the growth magnetic field, and θ the angle between the anisotropic magnetic easy axis and y-axis. ϕ_A indicates the angle between the direction of the average magnetization $\mathbf{m}_A$ of magnet *A* and the *x*-axis, and similarly, ϕ_B for magnet *B*.

In order to study the long-range magnetostatic interaction effect, we first obtain the equilibrium magnetization configuration in each magnet before applying a voltage to the multiferroic heterostructure. We next investigate the magnetization switching behavior of the two magnets at various neighboring distances in two successive switching steps. In switching step 1, an external electric voltage is applied to the PMN-PT substrate underneath magnet *B*, upon which a piezostrain is generated and transferred to magnet *B*. Then, the applied voltage is removed, allowing relaxation of the magnetization, defined as switching step 2. The stable magnetization states of the two magnets achieved during switching steps 1 and 2 are referred to as the strained states and the final states, respectively. We find that for each of the two switching steps, only when the separation distance is larger than a critical distance, an independent 90° magnetic switching for magnet *B* can be accomplished, which by definition is that the magnetization of magnet *B* switches by about 90° while that of magnet *A* almost remains still, within a 10° tolerance of rotation angles in our evaluation.

2. Method

In the phase-field model, the temporal evolution of the magnetization field **M** is simulated by solving the Landau–Lifshitz-Gilbert equation [26, 27, 65, 66], i.e.

$$\frac{\partial \mathbf{m}}{\partial t} = -\frac{\gamma_0}{1+\alpha^2}\left(\mathbf{m}\times\mathbf{H}_{\text{eff}} + \alpha\mathbf{m}\times(\mathbf{m}\times\mathbf{H}_{\text{eff}})\right), \quad (1)$$

where $\mathbf{m} = \mathbf{M}/M_S$ is the normalized magnetization field (M_S denoting saturated magnetization), and γ_0, α, and t are the gyromagnetic ratio of an electron, damping coefficient and time, respectively. The effective magnetic field $\mathbf{H}_{\text{eff}}$ is given by

$$\mathbf{H}_{\text{eff}} = -\frac{1}{\mu_0}\frac{\delta F}{\delta \mathbf{M}}. \quad (2)$$

Here, μ_0 represents the vacuum permeability. The total Helmholtz free energy F of the system as a function of the magnetization field within the two CoFeB magnetic nanoislands is expressed as [26, 27, 41]

$$F = \int \left(f_{\text{ms}} + f_{\text{exch}} + f_{\text{elastic}} + f_{\text{uni}} + f_{\text{external}}\right) dV. \quad (3)$$

f_{ms}, f_{exch}, f_{elastic}, f_{uni}, and f_{external} are the magnetostatic, exchange, elastic, uniaxial anisotropy, and external magnetic field energy densities, respectively.

The magnetostatic energy density is given by

$$f_{\text{ms}} = -\frac{1}{2}\mu_0 M_s \mathbf{H}_{\text{stray}}\cdot\mathbf{m}, \quad (4)$$

where $\mathbf{H}_{\text{stray}}$ is the stray field arising from both the magnetostatic interaction between the two magnets and that due to the inhomogeneity of the magnetization field within each magnet. $\mathbf{H}_{\text{stray}}$ is obtained by solving the magnetostatic equilibrium equation

$$\nabla\cdot(\mathbf{H}+\mathbf{M}) = 0. \quad (5)$$

The exchange energy density is calculated as

$$f_{\text{exch}} = A((\nabla m_1)^2 + (\nabla m_2)^2 + (\nabla m_3)^2), \quad (6)$$

where A is the exchange constant. The elastic energy density is given by

$$\begin{aligned} f_{\text{elastic}} &= \tfrac{1}{2}c_{ijkl}(\varepsilon_{ij}-\varepsilon^0_{ij})(\varepsilon_{kl}-\varepsilon^0_{kl}),\\ &= \tfrac{1}{2}(c_{11}(\varepsilon_{11}-\varepsilon^0_{11})^2 + c_{22}(\varepsilon_{22}-\varepsilon^0_{22})^2 + c_{33}(\varepsilon_{33}-\varepsilon^0_{33})^2)\\ &+c_{12}((\varepsilon_{11}-\varepsilon^0_{11})(\varepsilon_{22}-\varepsilon^0_{22}) + (\varepsilon_{11}-\varepsilon^0_{11})(\varepsilon_{33}-\varepsilon^0_{33})\\ &+(\varepsilon_{22}-\varepsilon^0_{22})(\varepsilon_{33}-\varepsilon^0_{33}))\\ &+2c_{44}((\varepsilon_{23}-\varepsilon^0_{23})^2 + (\varepsilon_{13}-\varepsilon^0_{13})^2 + (\varepsilon_{12}-\varepsilon^0_{12})^2), \end{aligned} \quad (7)$$

where c_{ijkl}, ε_{ij}, and ε^0_{ij} are the elastic stiffness tensor, total strain, and eigenstrain, respectively, and the Voigt notation is used to reduce the order of the elastic stiffness tensor. The eigenstrain is calculated as

$$\begin{aligned} &\varepsilon^0_{11} = \tfrac{3}{2}\lambda_{100}\left(m_1^2-\tfrac{1}{3}\right), \varepsilon^0_{22} = \tfrac{3}{2}\lambda_{100}\left(m_2^2-\tfrac{1}{3}\right),\\ &\varepsilon^0_{33} = \tfrac{3}{2}\lambda_{100}\left(m_3^2-\tfrac{1}{3}\right),\\ &\varepsilon^0_{12} = \tfrac{3}{2}\lambda_{111}\left(m_1m_2-\tfrac{1}{3}\right), \varepsilon^0_{13} = \tfrac{3}{2}\lambda_{111}\left(m_1m_3-\tfrac{1}{3}\right),\\ &\varepsilon^0_{23} = \tfrac{3}{2}\lambda_{111}\left(m_2m_3-\tfrac{1}{3}\right), \end{aligned} \quad (8)$$

Table 1. Material parameters of CoFeB used in the simulation.

Parameter	Value	Unit	Ref.
M_S	1.0×10^6	A m^{-1}	[73]
γ_0	1.76×10^{11}	Hz T^{-1}	[71]
λ_{110}	3.1×10^{-5}	/	[69]
λ_{111}	3.1×10^{-5}	/	[69]
α	0.005	/	[70]
c_{11}	2.8×10^{11}	N m^{-2}	[72]
c_{12}	1.4×10^{11}	N m^{-2}	[72]
c_{44}	0.7×10^{11}	N m^{-2}	[72]
K_{growth}	3500	J m^{-3}	[41]
A	1.5×10^{-11}	J m^{-1}	/

where λ_{100} and λ_{111} are the saturation magnetostriction along the $\langle 1\,0\,0\rangle$ and $\langle 1\,1\,1\rangle$ crystalline directions, respectively. According to Khachatuyan's microelasticity theory, the total strain is equal to the summation of the homogeneous strain $\overline{\varepsilon_{ij}}$ and the heterogeneous strain $\delta\varepsilon_{ij}$, i.e. $\varepsilon_{ij} = \overline{\varepsilon_{ij}} + \delta\varepsilon_{ij}$ [67, 68]. The distribution of the heterogeneous strain is solved from the mechanical equilibrium equation [34]. The homogeneous strain $\overline{\varepsilon_{ij}}$ represents the macroscopic deformation of the nanomagnet, which can be caused by the piezoelectric strain transferred from the piezoelectric substrate underneath (PMN-PT). The effective field orientation caused by $\overline{\varepsilon_{ij}}$ depends on both the anistropy of $\overline{\varepsilon_{ij}}$ and the sign of the magnetostrictive coefficients. For CoFeB nanomagnet with positive magnetostrictive coefficients (table 1), an effective field along x direction will be induced when $\overline{\varepsilon_{11}} - \overline{\varepsilon_{22}} > 0$, and it is along y direction if $\overline{\varepsilon_{11}} - \overline{\varepsilon_{22}} < 0$.

Following previous work [41], a uniaxial anisotropy due to the application of a magnetic field along the direction of the y-axis during the growth of the CoFeB magnets is considered, given by

$$f_{\text{uni}} = -K_{\text{growth}}m_2^2. \quad (9)$$

The external magnetic field energy density is written as

$$f_{\text{external}} = -\mu_0 M_s \mathbf{H}_{\text{ext}}\cdot\mathbf{m}, \quad (10)$$

where $\mathbf{H}_{\text{ext}}$ is the external magnetic field. In this work, we focus on pure voltage-controlled magnetization switching, thus $\mathbf{H}_{\text{ext}} = 0$ is used in the simulation.

The simulation system is set as $180\Delta x \times 90\Delta y \times 40\Delta z$ with a grid size of $\Delta x = \Delta y = 3$ nm and $\Delta z = 1$ nm. The in-plane dimension of the CoFeB nanoislands is 108 nm × 108 nm while the thicknesses of the CoFeB nanoislands and the PMN-PT substrate are 5 nm and 35 nm, respectively. The material parameters of CoFeB used in the phase-field simulation are listed in table 1 [41, 69–72]. All simulations were performed using the commercialized phase-field package μ-PRO®.

3. Results and discussions

3.1. Initial states

In a single CoFeB nanoisland grown on a PMN-PT substrate without an applied electric field or strain, the magnetization

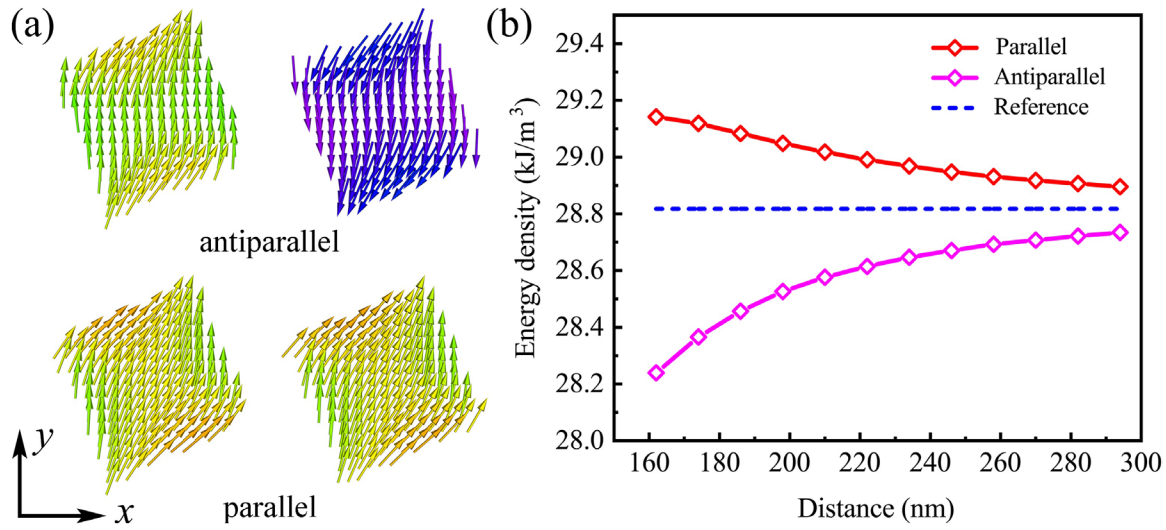

Figure 2. (a) Two initial magnetization configurations in the multiferroic heterostructure and (b) their free energy densities as a function of the neighboring distance R. The free energy density of an isolated single magnet is also presented for comparison.

has two energetically equivalent states at equilibrium: magnetization pointing up ($\phi \approx 77°$) and pointing down ($\phi \approx 257°$) [41]. For a group of two interactive magnets A and B, there might be four equilibrium magnetization states: (ϕ_A, ϕ_B) $\approx$ (77°, 77°), (77°, 257°), (257°, 77°), and (257°, 257°). They can be categorized into two types of magnetization states: the antiparallel state with opposite magnetization directions (ϕ_A, ϕ_B) $\approx$ (77°,257°) or (257°,77°) and the parallel state with same magnetization directions (ϕ_A, ϕ_B) $\approx$ (77°,77°) or (257°,257°). In the simulation, we use (ϕ_A, ϕ_B) $\approx$ (77°, 77°) and (77°, 257°) as examples for the parallel and antiparallel states, respectively, as depicted in figure 2(a). We find that both states can be stabilized, but they have different energies due to the interaction between them. As shown in figure 2(b), with the distances R between the two magnetic nanoislands increasing, the energy of the antiparallel state increases while the energy of the parallel state decreases, and both approach to the energy of an isolated single nanoisland. This indicates that the parallel state and the antiparallel state correspond to the meta-stable and stable states, respectively.

3.2. Switching from the antiparallel state to the parallel state

The functionality of a multiferroic heterostructure lies in the control of independent magnetization switching of each magnet, where each magnet should be able to accomplish a 180° switching under the effect of a piezoelectric strain transferred from its underlying substrate without altering the magnetization configuration of the other magnet. Since the two magnets in the heterostructure are equivalent to each other, we just need to simulate the 180°switching of one magnet (e.g. magnet B) of the two by applying an external electric field to it while keeping the other one (e.g. magnet A) under zero external electric field to study the interactions between them. Here we focus on the 180° switching of magnet B while keeping magnet A with an upward-pointing magnetization ($\phi_A \approx 77°$), which is the switching between an antiparallel state of (ϕ_A, ϕ_B) $\approx$ (77°, 257°) and a parallel state of (ϕ_A, ϕ_B) $\approx$ (77°, 77°). We first study the switching from the antiparallel state to the parallel state. This process involves two switching steps as defined above, which will be discussed in detail as following.

3.2.1. Switching step 1. Starting from the antiparallel state, an electric voltage is applied to the PMN-PT substrate beneath magnet B. Under the voltage, an anisotropic strain $\varepsilon_{11} - \varepsilon_{22}$ can be induced in the PMN-PT [43], whose magnitude depends on the strength of the applied voltage. Assuming that a strain anisotropy of $\varepsilon_{11} - \varepsilon_{22} = 1200$ ppm is generated on applying the voltage to the PMN-PT, which is the minimum strain required to switch the magnetization in the CoFeB/PMN-PT heterostructure with a single magnet, as identified in our simulation. We find that only when the neighboring distance R is greater than 174 nm can the magnetization be switched by the voltage-induced strain in magnet B independently. When the neighboring distance R is smaller than 174 nm, the system shows an obvious cross-talking effect: both magnetizations of A and B switch away from their initial configurations. For example, at $R = 156$ nm, which is about the closest possible neighboring distance for the chosen magnet size, the average magnetizations of A and B rotate by $\Delta\phi_A \approx 36°$ and $\Delta\phi_B \approx -76°$ (see figure 3(b)), respectively, with reference to the initial states in figure 3(a). For a larger neighboring distance $R \geqslant 174$ nm, the magnetization in magnet B rotates by $\Delta\phi_B \approx -90°$ while the magnetization configuration of magnet A almost remains the same as its initial state, as shown in figures 3(c) and (d).

The cross-talking behavior observed at $R < 174$ nm is attributed to the magnetostatic interaction between the two magnets. In this case, the magnetization in magnet B switches under the piezostrain transferred from the interface; meantime, the magnetization of magnet A is also switched due to the change in the magnetic stray field generated by magnet B. The stray field generated by magnet B (denoted by $\mathbf{H}^B_{\text{stray}}$) in the initial state and the strained state for $R = 156$ nm is shown in figures 4(a) and (b), respectively. In the initial state, the stray

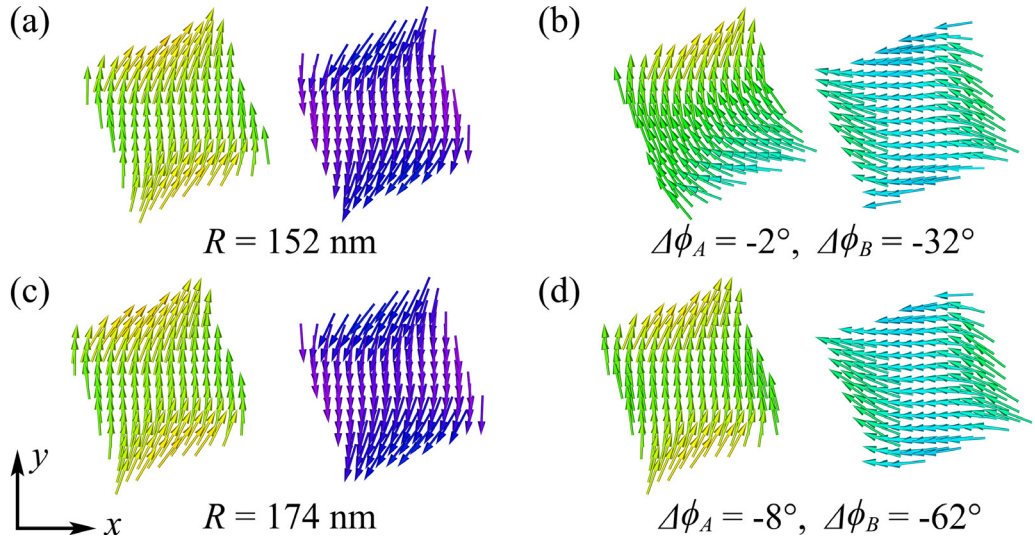

Figure 3. Magnetization configuration in (a) the initial state and (b) the strained state at the neighboring distance $R = 156$ nm as well as (c) the initial state and (d) the strained state at $R = 174$ nm during the antiparallel-to-parallel switching. $\Delta\phi_A$ and $\Delta\phi_B$ are the rotation angles of the average magnetization directions of magnets A and B between their initial states and straining state, respectively.

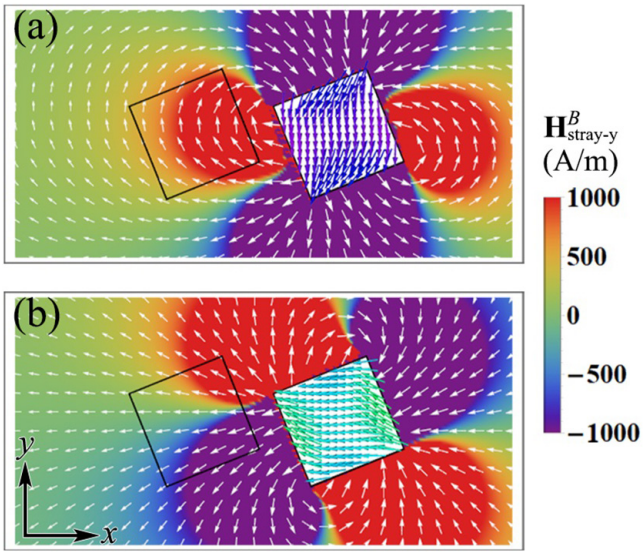

Figure 4. The magnetic stray field $\mathbf{H}^B_{\text{stray}}$ generated by magnet B in (a) the initial state and (b) the strained state, at $R = 156$ nm during the antiparallel-to-parallel switching. The black squares show the outline of the two magnets, while the color arrows inside magnet B indicate the magnetization field. The white arrows and the background color outside magnet B indicate the direction of $\mathbf{H}^B_{\text{stray}}$ and its component $H^B_{\text{stray-y}}$ (see the color bar), respectively.

field $\mathbf{H}^B_{\text{stray}}$ acting on magnet A is mostly along the y direction, with an average value of $\left\langle H^B_{\text{stray}\_x}\right\rangle_A = -550\,\text{A m}^{-1}$ and $\left\langle H^B_{\text{stray}\_y}\right\rangle_A = 1337\,\text{A m}^{-1}$, so the magnetization of magnet A is stabilized along the y direction. In the strained state, as accompanied by a 90° rotation of the magnetization of magnet B, the stray field $\mathbf{H}^B_{\text{stray}}$ acting on magnet A changes to the negative x direction, with an average value of $\left\langle H^B_{\text{stray}\_x}\right\rangle_A = -3250\,\text{A m}^{-1}$ and $\left\langle H^B_{\text{stray}\_y}\right\rangle_A = -393\,\text{A m}^{-1}$, causing the magnetization in A to rotate toward the negative x-axis from its initial state. The stray field $\mathbf{H}^B_{\text{stray}}$ acting on magnet A reduces upon increasing the neighboring distance R, and the magnetization switchings in the two magnets become decoupled at $R \geqslant 174$ nm. As a result, a criterion of $R \geqslant 174$ nm is required for an independent 90° switching of magnet B in switching step 1.

3.2.2. Switching step 2. A second 90° clockwise switching of magnet B upon removal of the external electric field in switching step 2 is required to accomplish a 180° magnetization rotation. We test different neighboring distances R following the criteria of $R \geqslant 174$ nm as required by the switching step 1. The strained and final magnetization configurations during switching step 2 of selected cases are shown in figures 5(a)–(f). According to the simulation, the magnetization configuration in magnet A is almost unaltered, while the magnetization in magnet B at the final state may have several different configurations, depending on the neighboring distance. For example, at $R = 174$ nm (figures 5(a) and (b)), the magnetization in B undergoes a slight clockwise rotation by an angle of $\Delta\phi_B' = -32.0°$. When the neighboring distance is $R = 186$ nm (figures 5(c) and (d)), the magnetization in B is stabilized at a curved structure with a rotation angle $\Delta\phi_B' = 62°$ from its initial state. When the neighboring distance increases to $R \geqslant 234$ nm (figures 5(e) and (f)), the magnetization in B can switch by ~90°. In combination with step 1, the magnetization completes a 180° switching from the antiparallel state to the parallel state.

The switching dependence on the neighboring distance R is again understood from the magnetostatic interaction between magnets A and B. At a small R, the magnetostatic interaction is strong, hindering the 90° magnetization switching of magnet B. Figures 6(a) and (b) show the stray fields $\mathbf{H}^A_{\text{stray}}$ generated by magnet A in the final states when R equals to 174 nm and 234 nm, respectively. In both cases, the stray field within the region of magnet B is nearly along the negative y direction, which hinders the magnetization from switching toward the

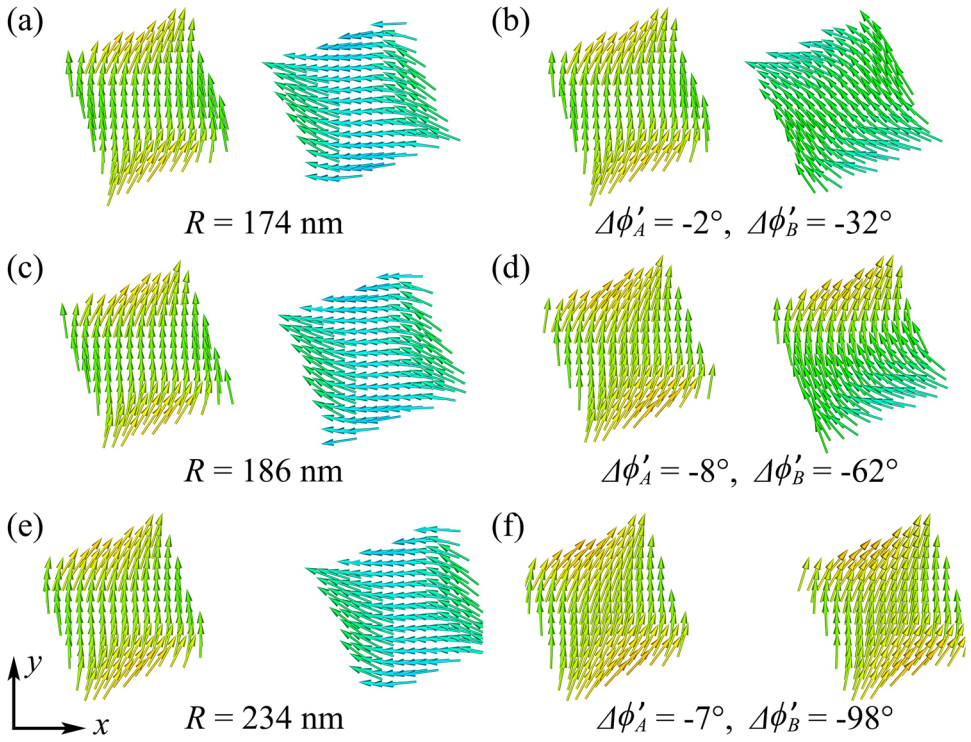

Figure 5. The magnetization configuration in (a) the strained state and (b) the final state at $R = 156$ nm, (c) the strained state and (d) the final state at $R = 186$ nm, as well as (e) the strained state and (f) the final state at $R = 234$ nm during the antiparallel-to-parallel switching, respectively. $\Delta\phi'_A$ and $\Delta\phi'_B$ are the rotation angles of the average magnetization directions of magnets A and B between their straining states and final states, respectively.

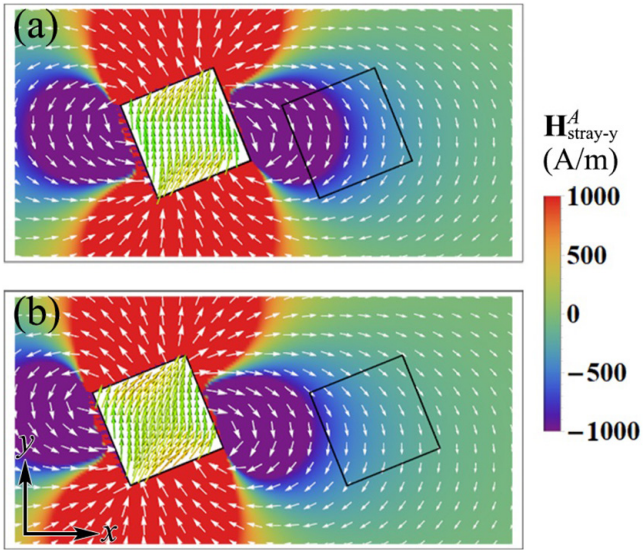

Figure 6. The stray magnetic field $\mathbf{H}^A_{\text{stray}}$ generated by magnet A at (a) $R = 174$ nm and (b) $R = 234$ nm during the antiparallel-to-parallel switching. The black squares show the outline of the two magnets, while the color arrows inside magnet A indicate the magnetization field. The white arrows and the background color outside magnet B indicate the direction of $\mathbf{H}^A_{\text{stray}}$ and its component $H^A_{\text{stray-y}}$ (see the color bar), respectively.

y direction. Furthermore, the stray field acting on magnet B reduces with R increasing, from $\langle H^A_{\text{stray-y}}\rangle_B = -954$ A m^{-1} at $R = 174$ nm to $\langle H^A_{\text{stray-y}}\rangle_B = -364$ A m^{-1} at $R = 234$ nm.

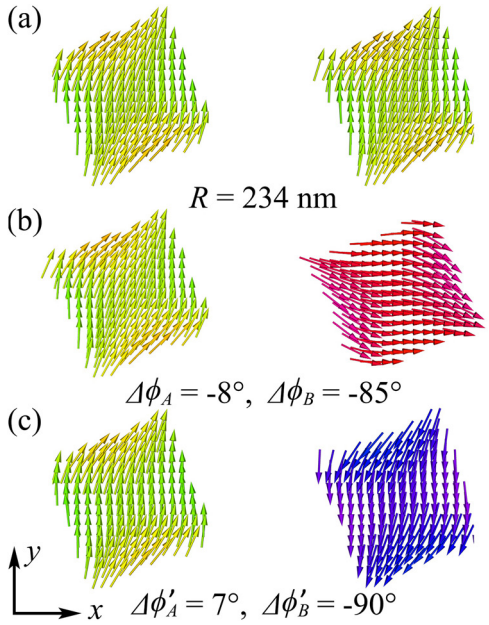

Figure 7. Magnetization configuration in (a) the initial state, (b) the strained state and (c) the final state at the neighboring distance $R = 234$ nm during the parallel-to-antiparallel switching.

Therefore, the 90° magnetization switching of magnet B can be achieved at $R \geqslant 234$ nm.

Based on the switching criteria for the two successive switching steps, a combined criterion for achieving an independent 180° magnetization switching in magnet B can be obtained: the neighboring distance R should be greater than

234 nm to assure a sufficiently weak magnetostatic interaction for decoupling the switching of the two magnets.

3.3. Switching from the parallel state to the antiparallel state

We next study the switching from the parallel state (ϕ_A, ϕ_B) ≈ (77°,77°) to the antiparallel state (ϕ_A, ϕ_B) ≈ (77°,257°). The results are shown in figures 7(*a*)–(*c*). We consider the critical neighboring distance of $R = 234$ nm. The simulation shows that a quasi-180° magnetization switching, $\Delta\phi_B = -85°$ in switching step 1 and $\Delta\phi_B' = -\ 90°$ in switching step 2, can be achieved in magnet *B*. Meanwhile, the magnetization in magnet *A* almost remains unchanged during the whole process. This suggests that the determinant factors of achieving electric-field-controlled 180° magnetization switching lie in the antiparallel-to-parallel process, which is reasonable because the antiparallel state is energetically more stable than the parallel state (discussed in section 3.1). Consequently, the switching from the parallel state to antiparallel state is easier than the reversed switching process.

4. Summary

In summary, we have investigated the electric-field-controlled magnetization switching in CoFeB/PMN-PT multiferroic heterostructures containing two interactive magnetic nanoislands using phase-field simulations. By simulating the magnetization configuration in the nanoislands during different switching steps, we identify a critical neighboring distance between the two magnetic nanoislands in order to achieve a 180° magnetization switching. Therefore, this work delivers an in-depth theoretical understanding on the effect of the magnetostatic interaction between two neighboring magnets on the electric-field-controlled magnetic switching. It is expected to provide valuable guidance for the fabrication and design of high-density multiferroic devices containing densely packed magnetic nanoislands.

Acknowledgments

This work at Tsinghua (M J Z and C W N) was supported by the NSF of China (Grant Nos. 51788104), China Scholarship Council (No 201706210108), National Science Foundation (Grant No. DMR-1744213), and the work at Penn State (T N Y, J J W and L Q C) is supported by the Army Research Office under Grant No. W911NF-17-1-0462. J J W and L Q C acknowledge the partial financial support for this effort from the Donald W Hamer Foundation through a Hamer Professorship at Penn State. The authors acknowledge support for computational resource from the Institute for CyberScience Advanced CyberInfrastructure (ICS-ACI) in The Pennsylvania State University. The authors also gratefully acknowledge the kind help with data visualization from Dr Chenglu Zhang at Tsinghua University.

ORCID iDs

Jian-Jun Wang https://orcid.org/0000-0002-9246-8916

References

[1] Tehrani S, Engel B, Chen E, DeHerrera M, Durlam M and Slaughter J M 2005 Recent developments in magnetic tunnel junction MRAM *INTERMAG 2000 Digest of Technical Papers. 2000 IEEE Int. Magnetics Conf.* vol 36 (IEEE) p 282
[2] Zhu J-G 2008 Magnetoresistive random access memory: the path to competitiveness and scalability *Proc. IEEE* **96** 1786–98
[3] Tehrani S *et al* 2003 Magnetoresistive random access memory using magnetic tunnel junctions *Proc. IEEE* **91** 703–12
[4] Hirohata A and Takanashi K 2014 Future perspectives for spintronic devices *J. Phys. D: Appl. Phys.* **47** 193001
[5] Jiles D C 2003 Recent advances and future directions in magnetic materials *Acta Mater.* **51** 5907–39
[6] Johnson M 2000 Magnetoelectronic memories last and last *IEEE Spectrosc.* **37** 33–40
[7] Fechner M, Zahn P, Ostanin S, Bibes M and Mertig I 2012 Switching magnetization by 180° with an electric field *Phys. Rev. Lett.* **108** 197206
[8] Cuellar F A *et al* 2014 Reversible electric-field control of magnetization at oxide interfaces *Nat. Commun.* **5** 4215
[9] Duan C-G, Jaswal S S and Tsymbal E Y 2006 Predicted magnetoelectric effect in Fe/$BaTiO_3$ multilayers: ferroelectric control of magnetism *Phys. Rev. Lett.* **97** 47201
[10] Chu Y-H *et al* 2008 Electric-field control of local ferromagnetism using a magnetoelectric multiferroic *Nat. Mater.* **7** 478–82
[11] Heron J T, Trassin M, Ashraf K, Gajek M, He Q, Yang S Y, Nikonov D E, Chu Y-H, Salahuddin S and Ramesh R 2011 Electric-field-induced magnetization reversal in a ferromagnet-multiferroic heterostructure *Phys. Rev. Lett.* **107** 217202
[12] Heron J T *et al* 2014 Deterministic switching of ferromagnetism at room temperature using an electric field *Nature* **516** 370–3
[13] Nan T *et al* 2015 Quantification of strain and charge co-mediated magnetoelectric coupling on ultra-thin permalloy/PMN-PT interface *Sci. Rep.* **4** 3688
[14] Nan T X, Zhou Z Y, Lou J, Liu M, Yang X, Gao Y, Rand S and Sun N X 2012 Voltage impulse induced bistable magnetization switching in multiferroic heterostructures *Appl. Phys. Lett.* **100** 132409
[15] Liu M, Hoffman J, Wang J, Zhang J, Nelson-Cheeseman B and Bhattacharya A 2013 Non-volatile ferroelastic switching of the Verwey transition and resistivity of epitaxial Fe_3O_4/PMN-PT (0 1 1) *Sci. Rep.* **3** 1876
[16] Zhang S *et al* 2015 Giant electrical modulation of magnetization in $Co_{40}Fe_{40}B_{20}$/$Pb(Mg_{1/3}Nb_{2/3})_{0.7}Ti_{0.3}O_3$ (0 1 1) heterostructure *Sci. Rep.* **4** 3727
[17] Franke K J A, López González D, Hämäläinen S J and van Dijken S 2014 Size dependence of domain pattern transfer in multiferroic heterostructures *Phys. Rev. Lett.* **112** 17201
[18] Bur A, Wong K, Zhao P, Lynch C S, Amiri P K, Wang K L and Carman G P 2011 Electrical control of reversible and permanent magnetization reorientation for magnetoelectric memory devices *Appl. Phys. Lett.* **98** 262504

[19] Finizio S *et al* 2014 Magnetic anisotropy engineering in thin film Ni nanostructures by magnetoelastic coupling *Phys. Rev. Appl.* **1** 21001
[20] Lahtinen T H E, Tuomi J O and Van Dijken S 2011 Pattern transfer and electric-field-induced magnetic domain formation in multiferroic heterostructures *Adv. Mater.* **23** 3187–91
[21] Rondinelli J M, Stengel M and Spaldin N A 2008 Carrier-mediated magnetoelectricity in complex oxide heterostructures *Nat. Nanotechnol.* **3** 46–50
[22] Weng Y, Lin L, Dagotto E and Dong S 2016 Inversion of ferrimagnetic magnetization by ferroelectric switching via a novel magnetoelectric coupling *Phys. Rev. Lett.* **117** 37601
[23] Vinai G *et al* 2019 Reversible modification of ferromagnetism through electrically controlled morphology *Adv. Electron. Mater.* **5** 1900150
[24] Hu J-M, Chen L-Q and Nan C-W 2016 Multiferroic heterostructures integrating ferroelectric and magnetic materials *Adv. Mater.* **28** 15–39
[25] Hu J-M, Duan C-G, Nan C-W and Chen L-Q 2017 Understanding and designing magnetoelectric heterostructures guided by computation: progresses, remaining questions, and perspectives *NPJ Comput. Mater.* **3** 18
[26] Peng R-C, Hu J-M, Momeni K, Wang J-J, Chen L-Q and Nan C-W 2016 Fast 180° magnetization switching in a strain-mediated multiferroic heterostructure driven by a voltage *Sci. Rep.* **6** 27561
[27] Wang J J, Hu J M, Ma J, Zhang J X, Chen L Q and Nan C W 2015 Full 180° magnetization reversal with electric fields *Sci. Rep.* **4** 7507
[28] Wang K L, Alzate J G and Khalili Amiri P 2013 Low-power non-volatile spintronic memory: STT-RAM and beyond *J. Phys. D: Appl. Phys.* **46** 74003
[29] Fusil S, Garcia V, Barthélémy A and Bibes M 2014 Magnetoelectric devices for spintronics *Annu. Rev. Mater. Res.* **44** 91–116
[30] Hu J M, Li Z, Chen L Q and Nan C W 2012 Design of a voltage-controlled magnetic random access memory based on anisotropic magnetoresistance in a single magnetic layer *Adv. Mater.* **24** 2869–73
[31] Hu J-M and Nan C W 2009 Electric-field-induced magnetic easy-axis reorientation in ferromagnetic/ferroelectric layered heterostructures *Phys. Rev.* B **80** 224416
[32] Yang S, Feng L, Zhang D, Huang W, Dong S, Wang J, Zou L, Li X and Nan C 2015 Magnetically correlated anisotropic resistive switching manipulated by electric field in Co/PMN-PT heterostructures *J. Alloys Compd.* **646** 472–6
[33] Hu J-M, Li Z, Chen L-Q and Nan C-W 2011 High-density magnetoresistive random access memory operating at ultralow voltage at room temperature *Nat. Commun.* **2** 553
[34] Wang J-J, Yang T-N, Zorn J A, Wang E, Irwin J, Lindemann S, Rzchowski M S, Hu J-M, Eom C-B and Chen L-Q 2019 Strain anisotropy and magnetic domain structures in multiferroic heterostructures: High-throughput finite-element and phase-field studies *Acta Mater.* **176** 73–83
[35] Lahtinen T H E, Franke K J A and van Dijken S 2012 Electric-field control of magnetic domain wall motion and local magnetization reversal *Sci. Rep.* **2** 258
[36] Skumryev V, Laukhin V, Fina I, Martí X, Sánchez F, Gospodinov M and Fontcuberta J 2011 Magnetization reversal by electric-field decoupling of magnetic and ferroelectric domain walls in multiferroic-based heterostructures *Phys. Rev. Lett.* **106** 57206
[37] Chen Y, Fitchorov T, Vittoria C and Harris V G 2010 Electrically controlled magnetization switching in a multiferroic heterostructure *Appl. Phys. Lett.* **97** 52502
[38] Kundu A A, Chavez A C, Keller S M, Carman G P and Lynch C S 2018 360° deterministic magnetization rotation in a three-ellipse magnetoelectric heterostructure *J. Appl. Phys.* **123** 104105
[39] Yang S-W, Peng R-C, Jiang T, Liu Y-K, Feng L, Wang J-J, Chen L-Q, Li X-G and Nan C-W 2014 Non-volatile 180° magnetization reversal by an electric field in multiferroic heterostructures *Adv. Mater.* **26** 7091–5
[40] Biswas A K, Ahmad H, Atulasimha J and Bandyopadhyay S 2017 Experimental demonstration of complete 180° reversal of magnetization in isolated Co nanomagnets on a PMN-PT substrate with voltage generated strain *Nano Lett.* **17** 3478–84
[41] Peng R-C, Wang J J, Hu J-M, Chen L-Q and Nan C-W 2015 Electric-field-driven magnetization reversal in square-shaped nanomagnet-based multiferroic heterostructure *Appl. Phys. Lett.* **106** 142901
[42] Gilbert I, Chavez A C, Pierce D T, Unguris J, Sun W-Y, Liang C-Y and Carman G P 2016 Magnetic microscopy and simulation of strain-mediated control of magnetization in PMN-PT/Ni nanostructures *Appl. Phys. Lett.* **109** 162404
[43] Buzzi M, Chopdekar R V, Hockel J L, Bur A, Wu T, Pilet N, Warnicke P, Carman G P, Heyderman L J and Nolting F 2013 Single domain spin manipulation by electric fields in strain coupled artificial multiferroic nanostructures *Phys. Rev. Lett.* **111** 27204
[44] Wang J-J and Chen L-Q 2018 Strain control of domain structures in ferroelectric thin films: applications of phase-field method *Handbook of Materials Modeling* (Cham: Springer) pp 1–18
[45] Chen L-Q 2002 Phase-field models for microstructure evolution *Annu. Rev. Mater. Res.* **32** 113–40
[46] Wang J and Zhang J 2013 A real-space phase field model for the domain evolution of ferromagnetic materials *Int. J. Solids Struct.* **50** 3597–609
[47] Li L J, Lei C H, Shu Y C and Li J Y 2011 Phase-field simulation of magnetoelastic couplings in ferromagnetic shape memory alloys *Acta Mater.* **59** 2648–55
[48] Li J-Y, Lei C-H, Li L-J, Shu Y-C and Liu Y-Y 2012 Unconventional phase field simulations of transforming materials with evolving microstructures *Acta Mech. Sin.* **28** 915–27
[49] Wang J 2019 Mechanical control of magnetic order: from phase transition to skyrmions *Annu. Rev. Mater. Res.* **49** 361–88
[50] Wang J-J, Wang B and Chen L-Q 2019 Understanding, predicting, and designing ferroelectric domain structures and switching guided by the phase-field method *Annu. Rev. Mater. Res.* **49** 127–52
[51] Yang T N, Hu J-M, Nan C W and Chen L Q 2014 Predicting effective magnetoelectric response in magnetic-ferroelectric composites via phase-field modeling *Appl. Phys. Lett.* **104** 52904
[52] Wang J J, Hu J M, Peng R-C, Gao Y, Shen Y, Chen L Q and Nan C W 2015 Magnetization reversal by out-of-plane voltage in $BiFeO_3$-based multiferroic heterostructures *Sci. Rep.* **5** 10459
[53] Wang J J, Hu J M, Yang T N, Feng M, Zhang J X, Chen L Q and Nan C W 2015 Effect of strain on voltage-controlled magnetism in $BiFeO_3$-based heterostructures *Sci. Rep.* **4** 4553
[54] Wang J J, Eliseev E A, Ma X Q, Wu P P, Morozovska A N and Chen L Q 2011 Strain effect on phase transitions of $BaTiO_3$ nanowires *Acta Mater.* **59** 7189–98
[55] Wang B, Chen H-N, Wang J-J and Chen L 2019 Ferroelectric domain structures and temperature-misfit strain phase diagrams of $K_{1-x}Na_xNbO_3$ thin films: a phase-field study *Appl. Phys. Lett.* **115** 92902
[56] Zhou M-J, Wang J-J, Chen L-Q and Nan C-W 2018 Strain, temperature, and electric-field effects on the phase

transition and piezoelectric responses of $K_{0.5}Na_{0.5}$ Nb_3 thin films *J. Appl. Phys.* **123** 154106
[57] Sheng G, Zhang J X, Li Y L, Choudhury S, Jia Q X, Liu Z K and Chen L Q 2008 Domain stability of $PbTiO_3$ thin films under anisotropic misfit strains: phase-field simulations *J. Appl. Phys.* **104** 54105
[58] Wang J J, Hu J-M, Chen L-Q and Nan C-W 2013 Strain-domain structure and stability diagrams for single-domain magnetic thin films *Appl. Phys. Lett.* **103** 142413
[59] Li P W *et al* 2017 Spatially resolved ferroelectric domain-switching-controlled magnetism in $Co_{40}Fe_{40}B_{20}$/$Pb(Mg_{1/3}Nb_{2/3})_{0.7}Ti_{0.3}O_3$ multiferroic heterostructure *ACS Appl. Mater. Interfaces* **9** 2642–9
[60] Zhang S *et al* 2012 Electric-field control of nonvolatile magnetization in $Co_{40}Fe_{40}B_{20}$/$Pb(Mg_{1/3}Nb_{2/3})_{0.7}Ti_{0.3}O_3$ structure at room temperature *Phys. Rev. Lett.* **108** 137203
[61] Li P, Chen A, Li D, Zhao Y, Zhang S, Yang L, Liu Y, Zhu M, Zhang H and Han X 2014 Electric field manipulation of magnetization rotation and tunneling magnetoresistance of magnetic tunnel junctions at room temperature *Adv. Mater.* **26** 4320–5
[62] Chen A *et al* 2016 Angular dependence of exchange bias and magnetization reversal controlled by electric-field-induced competing anisotropies *Adv. Mater.* **28** 363–9
[63] Liu Y *et al* 2016 Electric-field control of magnetism in $Co_{40}Fe_{40}B_{20}/(1-x)Pb(Mg_{1/3}Nb_{2/3})O_{3-x}PbTiO_3$ multiferroic heterostructures with different ferroelectric phases *ACS Appl. Mater. Interfaces* **8** 3784–91
[64] Chen A *et al* 2019 Giant nonvolatile manipulation of magnetoresistance in magnetic tunnel junctions by electric fields via magnetoelectric coupling *Nat. Commun.* **10** 243
[65] Yang T N, Hu J-M, Nan C W and Chen L Q 2014 On the elastically coupled magnetic and ferroelectric domains: a phase-field model *Appl. Phys. Lett.* **104** 202402
[66] Zhang J X and Chen L Q 2005 Phase-field microelasticity theory and micromagnetic simulations of domain structures in giant magnetostrictive materials *Acta Mater.* **53** 2845–55
[67] Wang J J, Ma X Q, Li Q, Britson J and Chen L Q 2013 Phase transitions and domain structures of ferroelectric nanoparticles: Phase field model incorporating strong elastic and dielectric inhomogeneity *Acta Mater.* **61** 7591–603
[68] Khachaturyan A G 1983 *Theory of Structural Transformations in Solids* (New York: Wiley)
[69] Wang D, Nordman C, Qian Z, Daughton J M and Myers J 2005 Magnetostriction effect of amorphous CoFeB thin films and application in spin-dependent tunnel junctions *J. Appl. Phys.* **97** 10C906
[70] Liu X, Zhang W, Carter M J and Xiao G 2011 Ferromagnetic resonance and damping properties of CoFeB thin films as free layers in MgO-based magnetic tunnel junctions *J. Appl. Phys.* **110** 33910
[71] Liu L, Pai C-F, Li Y, Tseng H W, Ralph D C and Buhrman R A 2012 Spin-torque switching with the giant spin Hall effect of tantalum *Science* **336** 555–8
[72] Pertsev N A 2013 Origin of easy magnetization switching in magnetic tunnel junctions with voltage-controlled interfacial anisotropy *Sci. Rep.* **3** 2757
[73] Burrowes C *et al* 2013 Low depinning fields in Ta–CoFeB–MgO ultrathin films with perpendicular magnetic anisotropy *Appl. Phys. Lett.* **103** 182401